Materials Today Communications 33 (2022) 104724

Contents lists available at ScienceDirect

Materials Today Communications

journal homepage: www.elsevier.com/locate/mtcomm

Additive manufacturing of novel heterostructured martensite-austenite dual-phase steel through in-situ alloying

Jinlong Su [a,b], Chaolin Tan [a,*], Fern Lan Ng [a], Fei Weng [a], Lequn Chen [a], Fulin Jiang [b], Jie Teng [b,*], Youxiang Chew [a,*]

[a] Singapore Institute of Manufacturing Technology, A*STAR, 5 Cleantech Loop, 636732, Singapore
[b] College of Materials Science and Engineering, Hunan University, Changsha 410082, China

ARTICLE INFO

Keywords:
Additive manufacturing
Dual-phase steel
In-situ alloying
Heterogeneous microstructure
Mechanical properties

ABSTRACT

The interplay between the martensite and austenite phases in steel has critical effects on the mechanical properties. To tune the phase constitutions of martensite and austenite phases, this work in-situ alloyed martensitic C300 maraging steel (MS) with austenitic 316 L stainless steel (SS) laser-directedected energy deposition (LDED). The microstructures, mechanical properties and deformation behaviour of the novel MS-12 wt. % SS (MS12) and MS-24 wt. % SS (MS24) dual-phase steels were investigated. The as-built samples achieve a relative density above 99.9 % and martensite-austenite dual-phase heterostructures. Micro-segregation of molybdenum is considered the dominant reason for the face-centred cubic (FCC) phase formation. The fractions of the FCC phase were 5.8 % and 16.8 % in the MS12 and MS24 alloys, respectively. Moreover, the unique thermal history of LDED induces the heterostructured microstructure with FCC-rich and FCC-lean regions, which contributes to the high work hardenability of the steel. Compared with MS12, MS24 shows a much higher elongation (14.3 %) and a superior work-hardening capability. The in-situ digital image correlation (DIC) observations reveal the strain partitioning within the two alloys during the initial deformation stage. The findings highlight a new approach to developing new materials by in-situ alloying commercially available materials using LDED.

1. Introduction

Additive manufacturing has gained growing interest in recent years because the innovative technology possesses many unique advantages, including freedom in composition design, high efficiency in material usage and reduced manufacturing life-cycle [1–3]. Performing laser-directed energy deposition (LDED) with in-situ alloying is widely adopted as a cost-efficient processing method to achieve desirable alloy composition through mixing different types of elemental powders and/or pre-alloyed powders [4]. Benefiting from the Marangoni convection incited by localised high laser energy intensity, the multiple materials are well mixed in the melt pool, forming homogeneous materials without evident elemental segregation [5].

Dual-phase (DP) steels with soft and hard phases are promising structural materials due to the good combination of strength, ductility and superior work-hardening capability [6,7]. The superior work-hardening capability of DP steels stems from the superior strain hardening behaviour of the softer phase through the introduction of deformation twining, strain partitioning or strain-induced phase transformation [7–9]. However, constrained by the high cost of pre-alloyed powders, the research on the additive manufacturing of martensite-austenite DP steels is seldom reported. As such, LDED combined with in-situ alloying seems to be a feasible method to achieve DP steels with martensite-austenite microstructure.

Currently, the research on additive manufacturing of DP steels is mainly focused on the ferrite-austenite duplex stainless steels [10]. For instance, Hengsbach et al. [11] investigated the microstructure and mechanical properties of the laser powder bed fusion (LPBF) processed UNS S31803 duplex stainless steel, and the as-built alloy is mainly ferritic with a minor austenite phase, where a post-heat treatment procedure is necessary to achieve the desirable dual-phase microstructure. Li et al. [12] reported that the ferrite-austenite duplex microstructures could be achieved through LPBF combined with in-situ alloying 22Cr duplex stainless steel (SAF2205) powders with Ni powders. Ni is an austenite stabiliser and thereby promoting the formation of austenite in those melt pools rich in Ni. The research regarding the fabrication of

* Corresponding authors.
E-mail addresses: tclscut@163.com (C. Tan), tengjie@hnu.edu.cn (J. Teng), chewyx@simtech.a-star.edu.sg (Y. Chew).

https://doi.org/10.1016/j.mtcomm.2022.104724
Received 14 June 2022; Received in revised form 20 September 2022; Accepted 18 October 2022
Available online 19 October 2022

Table 1
Chemical composition of the feedstock materials.

Element (wt. %)	Ni	Co	Mo	Ti	Mn	Cr	Si	C	Fe
C300 MS	18.3	9.1	4.9	0.75	0.04	0.09	0.1	0.01	Bal.
316L SS	12.6	–	2.5	–	1.6	17.1	0.8	0.013	Bal.

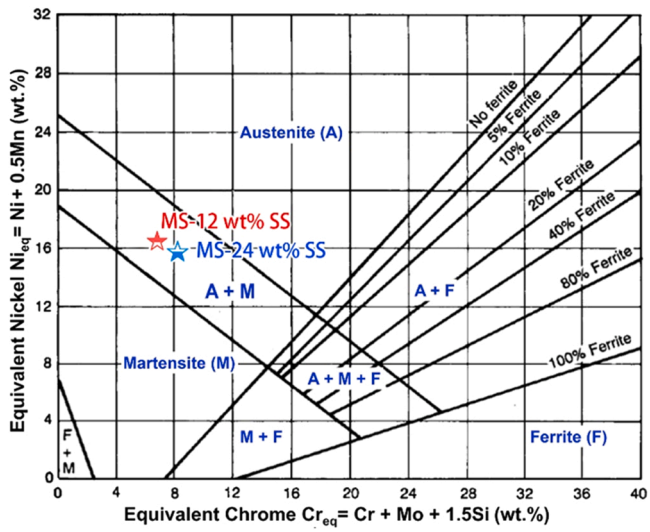

Fig. 1. Schaeffler-Delong diagram predicts phase compositions of MS-SS alloys based on their Ni and Cr equivalent values [15].

martensite-austenite DP steels by additive manufacturing is still lacking [13]. As a result, the aim of the present work is focused on the additive manufacturing of DP steels through LDED combined with in-situ alloying.

Recently, Ben-Artzy et al. [14] investigated the joint between C300 maraging steel with 316 L stainless steel processed by LDED, and reported that dual-phase microstructure can be obtained at the transition region without the formation of intermetallic phases. Hence, the C300 maraging steel and 316 L stainless steel were selected as the feedstock materials in the present work. The C300 maraging steel (MS) is typical martensite steel, while the 316 L stainless steel (SS) is typical austenitic steel. Two types of alloy compositions were processed, and their microstructure characteristics were analysed by optical microscopy (OM), electron backscattered diffraction (EBSD) and energy-dispersive X-ray spectroscopy (EDS). Moreover, tensile tests, along with a digital image correlation (DIC) system, were adopted to investigate the mechanical properties and deformation behaviour of the DP steels.

2. Experimental procedure

Commercial martensitic grade 300 maraging steel powder and austenitic 316 L stainless steel powder produced by vacuum gas atomisation were selected as the feedstock material, and the chemical compositions are listed in Table 1. The alloy composition design of MS-SS alloys is based on the Schaeffler-Delong diagram prediction, as exhibited in Fig. 1. According to the prediction, the typical martensite-austenite dual-phase microstructure could be achieved under two alloying compositions of MS12 and MS24.

The schematic diagram of the in-situ alloying LDED process is presented in Fig. 2a, and the powder morphologies of MS and SS powders are presented in Fig. 2b. The average particle sizes of MS and SS are about 40 and 42 μm, respectively. The MS12 and MS24 alloys were deposited using the powder-blown LDED system (developed by the Singapore Institute of Manufacturing Technology) under the optimised processing parameters, i.e., laser scan speed 1200 mm/min, laser power 850 W and hatch space 0.65 mm. The gross powder feeding rate is about 2.8 g/min [16]. Moreover, pure Ar gas (>99.999 %) was adopted to deliver the mixed powders from the hoppers to the coaxial nozzle and shield the melt pool, as exhibited in Fig. 2a. The gas flow rate of shielding gas and carrier gas was 15 L/min and 5 L/min, respectively. Two hoppers with MS and SS powders feedstock material were utilised. During the fabricating process, mixed powders are carried by the pure Ar gas and blended in the tube and splitter. The deposited blocks of MS12 and MS24 alloys are about 75 mm × 50 mm× 6 mm (Fig. 2c).

Samples for microstructure observations were sectioned along the build direction. The porosity was determined from optical microscopy (OM) images captured at × 25 using the ImageJ software. The samples for microstructure observations were etched in a 3 % Nital etchant for 20 s. The grain orientation and phase distribution of alloy samples were analysed by EBSD using a step size of 0.3 μm operated at the accelerating voltage of 20 kV. AZtecCrystal software was used to analyse the acquired EBSD data. The mechanical properties were measured using an Instron 5982 universal material testing machine with a loading speed of

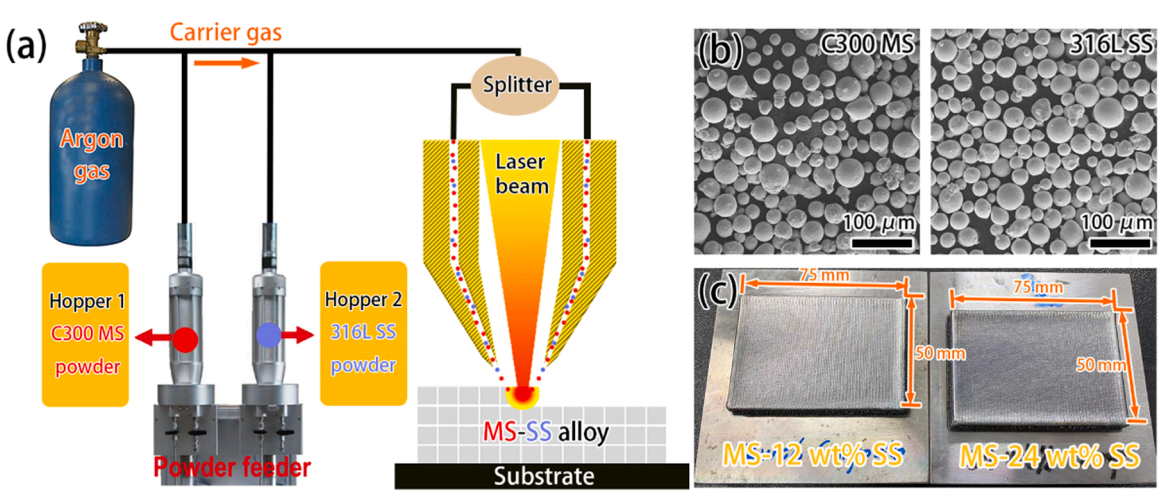

Fig. 2. Experimental details. (a) Schematic diagram of LDED in-situ alloying of MS and SS with two hoppers, (b) SEM morphologies of the MS and SS powders, and (c) LDED-built MS12 and MS24 blocks.

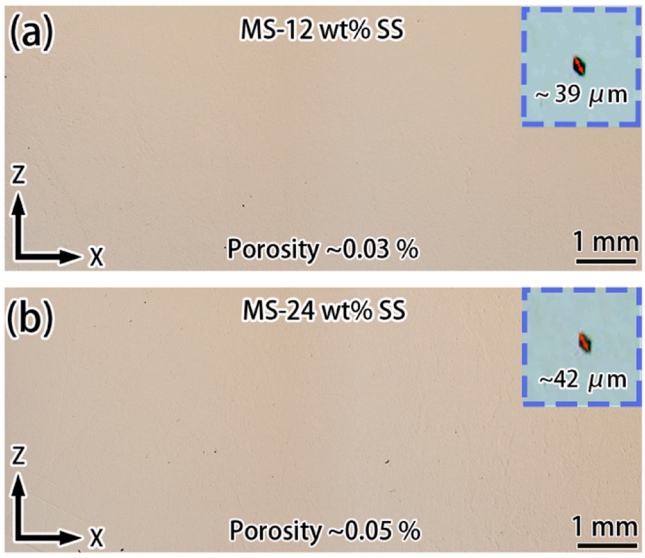

Fig. 3. OM images of the polished (a) MS12 and (b) MS24 samples taken from the X-Z cross-sections show a high relative density (Z parallel to build direction).

1 mm/min. During tensile tests, a 2D digital image correlation (DIC) system along with the ZEISS GOM correlate software was used for in-situ monitoring of the localised strain and failure behaviour. A FLIR Grasshopper3 CCD camera was used to capture the images of sample deformation at 2 frames/second during tensile tests. The gauge size of the tensile coupon is $20 \times 6 \times 2.5$ mm^3.

3. Results

The OM images of the polished MS12 and MS24 samples were presented in Fig. 3. Only a few pores can be found within the two as-built alloys without other observable defects, demonstrating the good processing parameters and high density in the as-built samples. The maximum pore diameter was 39 and 42 μm, respectively, for MS12 and MS24 alloys. Moreover, the porosity of MS12 and MS24 alloys were estimated to be ~0.03 % and 0.05 %, suggesting a high relative density of 99.97 % and 99.95 %, respectively.

The microstructures of MS12 and MS24 samples observed at X-Z cross-sections were presented in Fig. 4. Melt pools profile features are evident in two samples, as shown in Fig. 4a and c. Moreover, cellular and dendritic microstructure coexisted in two samples, which is similar to typical additively manufactured martensite steel [17,18]. The mixed microstructures (cellular and dendritic) were caused by the different thermal histories experienced in different localised regions. These microstructures were determined by the combined effects of thermal gradient (G) and solidification rate (R). Generally, the higher G/R ratio promotes the formation of cellular structure, while the lower G/R ratio promotes dendritic structure formation [19]. In addition, the size of the cellular and dendritic structure of the MS24 alloy is larger than that of the MS12 alloy, which could be related to the different transformation behaviour within the two alloys. It can be inferred that the higher content of SS brings more austenite stabilising elements (e.g., Cr and Mn), which retard the austenite (γ)→martensite (α') transformations during deposition, and thereby coarsening the cellular and dendritic structure.

Fig. 5 shows the EBSD and corresponding EDS results of the vertical cross-sections of MS12 alloy. As shown in Fig. 5a, the inverse pole figure (IPF) map reveals the random orientation of the grains. According to the phase map in Fig. 5b, typical martensite/austenite dual-phase microstructure was achieved in MS12 alloy, and the fraction of FCC phase is

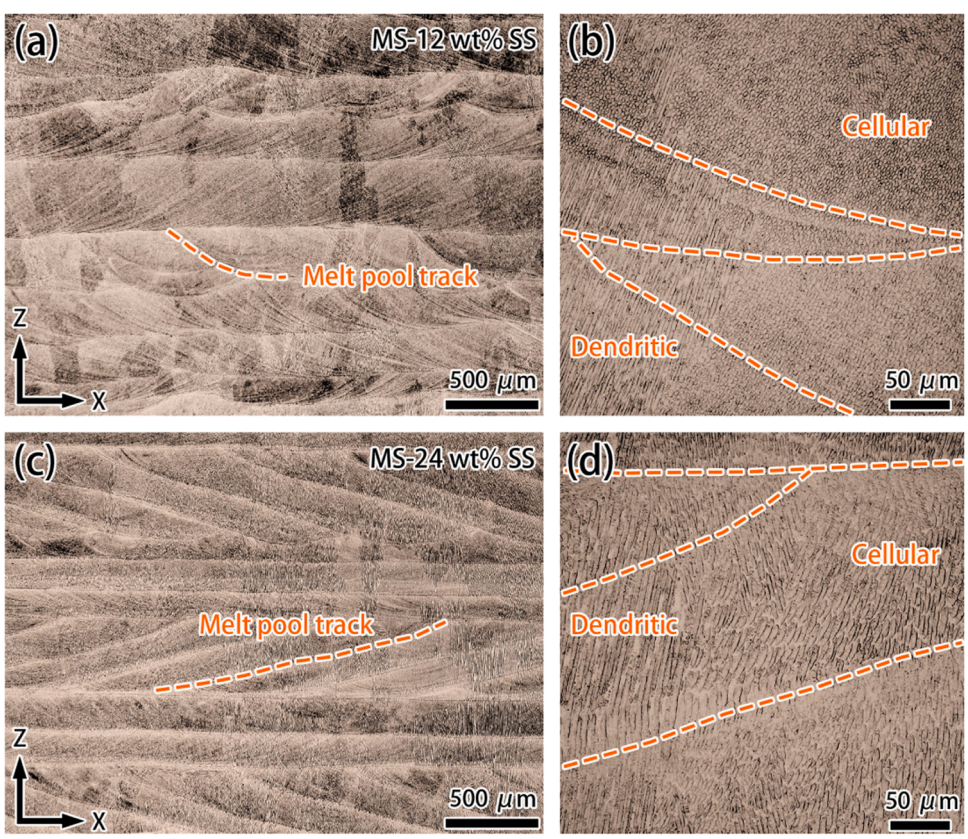

Fig. 4. Microstructures of the MS-SS alloy samples observed at X-Z cross-sections: (a) and (b) MS12, and (c) and (d) MS24.

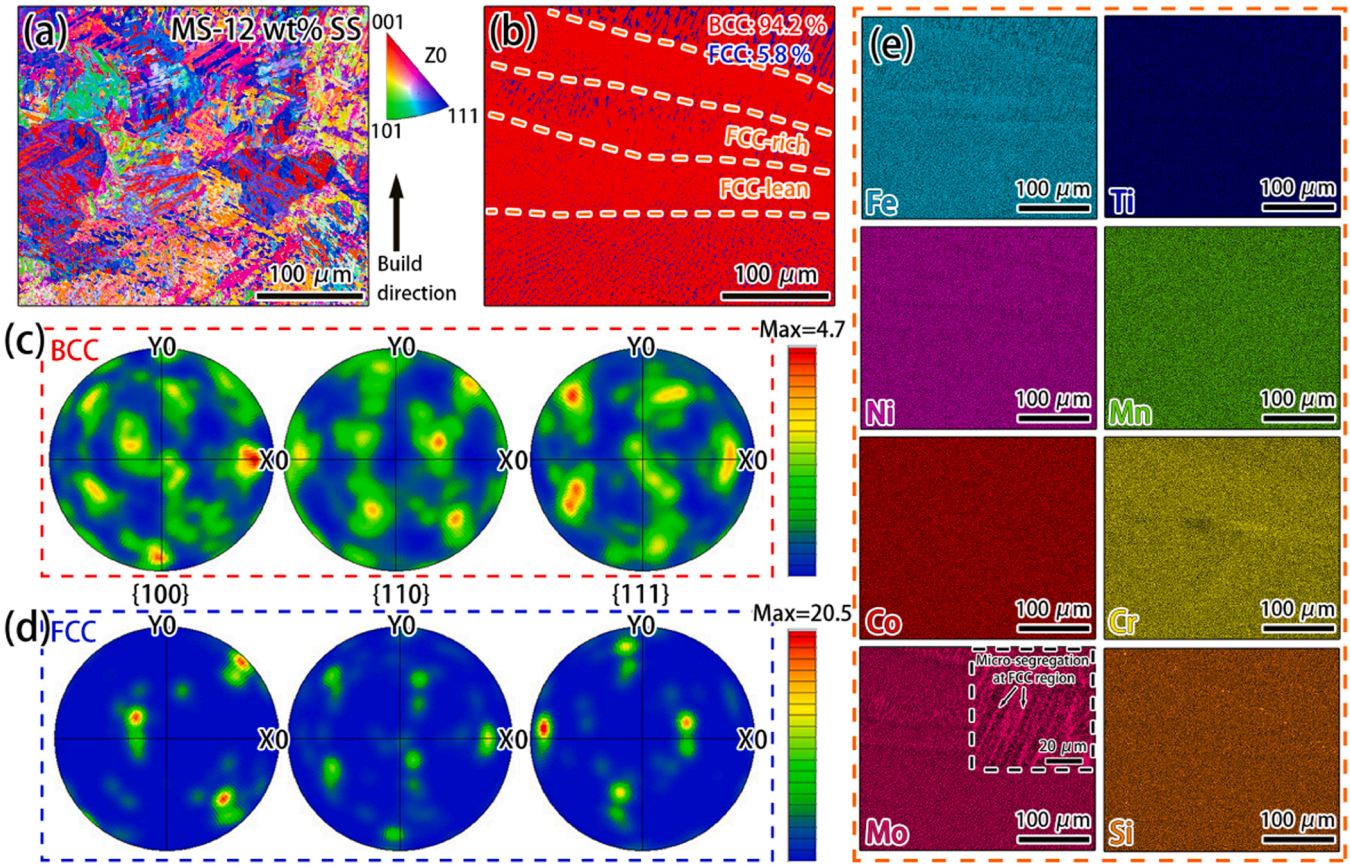

Fig. 5. EBSD and EDS investigations of MS12 alloy along build direction. (a) IPF map, (b) phase distribution map, pole figures of (c) BCC and (d) FCC phase, (e) EDS results.

about 5.8 %. Moreover, the spatial heterostructures with alternating FCC-rich and FCC-lean regions are observed within the alloy. Note that the cooling rate at the bottom of the melt pool is relatively higher during deposition. The FCC-lean regions between the deposited layers could be attributed to the higher cooling rate in those regions, promoting the $\gamma \rightarrow \alpha'$ transformation and thereby retard the formation of the FCC phase. In addition, it can be found in Fig. 5b that the FCC phase was mainly distributed in the inter-dendritic region rather than the inter-cellular region. This can be well understood as the lower solidification rate at the inter-dendritic regions promotes the formation of the FCC phase [13]. To investigate the crystallographic texture of the two phases, the pole figures of the body-centered cubic (BCC) and FCC phase were presented in Fig. 5c and d, respectively. Compared to the FCC phase, the maximum multiple of uniform density (MUD) of BCC is much higher, which can be attributed to the considerably fewer data points in this phase [20]. Moreover, the Kurdjumov-Sachs (K-S) orientation relationship ($\{111\}_{\gamma}//\{011\}_{\alpha'}$) between the BCC and FCC phase can be observed in the pole figures in Fig. 5c and d [21]. A similar phenomenon has also been observed between lath martensite and retained austenite grains in conventionally heat-treated maraging steels [22]. The EDS results in Fig. 5e indicated that the alloying elements were in uniform distribution, and only the Mo element showed obvious micro-segregation, demonstrating the good homogeneity of the in-situ alloying processing method.

Fig. 6 shows the EBSD and corresponding EDS results of the vertical cross-sections of MS24 alloy. The EDS results of as-built MS-SS alloy blocks are listed in Table 2. As shown in Fig. 6b, the FCC phase fraction in MS24 alloy reaches 16.8 %, suggesting that the higher content of SS promotes the formation of the FCC phase. Moreover, a more apparent heterostructured microstructure with FCC-rich and FCC-lean regions in the alloy was achieved. The FCC phase was also distributed in the inter-cellular/dendritic regions. Different from MS12 alloy, the columnar γ grains were obtained within MS24 alloy, as shown in Fig. 6a. Meanwhile, the pole figures in Fig. 6c show that the MUD of martensite (i.e., 9.2) in MS24 alloy was higher than that of MS12 alloy (i.e., 4.7). The particular phenomenon is related to the different phase transformation behaviour in two types of steels, which will be discussed in the following section. In addition, micro-segregation of Mo was also observed in the inter-cellular/dendritic regions (i.e. FCC regions) according to the EDS analysis in Fig. 6e, which indicates that the formation of the FCC phase could be related to the micro-segregation of Mo element.

The engineering tensile stress-strain curves and corresponding tensile data of the MS-SS alloys are presented in Fig. 7a. Compared with MS12 alloy, MS24 alloy shows a lower yield strength (YS) but higher elongation. Meanwhile, the ultimate tensile strength (UTS) of the two alloys does not differ significantly. The tensile strength and elongation of MS24 alloy are 873.2 ± 32.8 MPa, and 14.3 ± 1.3 %, respectively. Moreover, the true stress-strain curves of the two alloys are given in Fig. 7b (the necking stage has been removed). Combining both the work-hardening rate curves in Fig. 7b, a higher work-hardening rate and a more stable work-hardening stage are achieved in MS24 alloy, suggesting a superior work-hardening ability and ductility of the alloy.

DIC measurements were utilised to investigate the plastic deformation behaviour of the MS-SS alloys. As shown in Fig. 8a and d, strain partitioning was observed within the two alloys at the initial stage of deformation (strain=2 %) [23]. The FCC-rich region with lower yield stress could be deformed first during tensile tests, and the strain partitioning could contribute to the work-hardening capability of the MS-SS alloys. Regarding the fracture behaviour, different fracture features were observed in the two alloys. The maximum strain site in MS12 alloy originated from the centre of the sample (Fig. 8b), and the typical 45° shear fracture morphology was formed, which is the maximum resolved

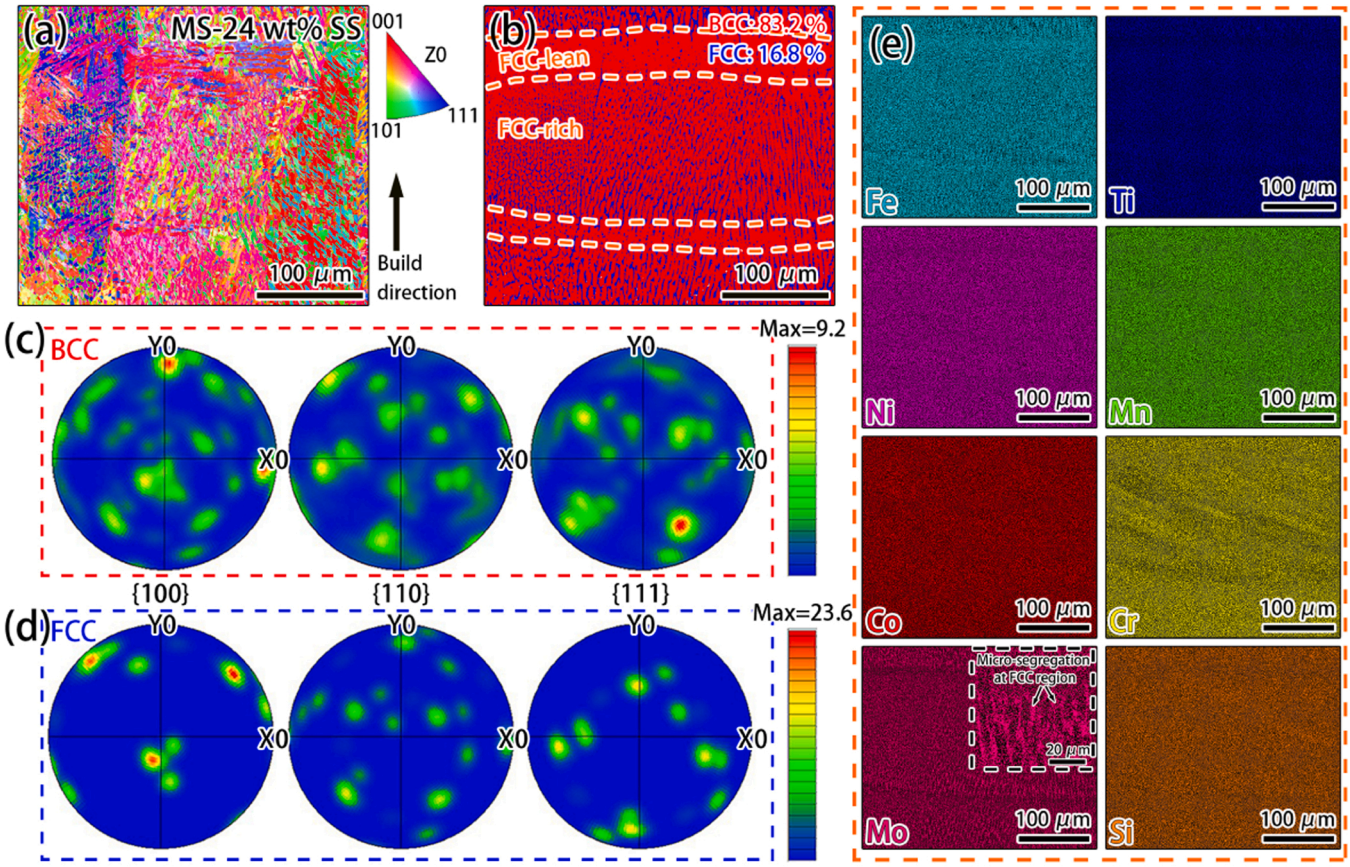

Fig. 6. EBSD and EDS investigations of MS24 alloy along build direction. (a) IPF map, (b) phase distribution map, pole figures of (c) BCC and (d) FCC phase, (e) EDS results.

Table 2
EDS results of as-built MS-SS alloy blocks.

Element (wt. %)	Ni	Co	Mo	Ti	Mn	Cr	Si	Fe
MS12	16.38	8.08	4.23	0.91	0.17	2.36	0.15	Bal.
MS24	15.57	7.02	3.69	0.79	0.26	4.2	0.2	Bal.

shear stress to the tensile force. However, for MS24 alloy, the crack gradually propagated along the transverse direction (as shown in the inset of Fig. 8f). After the fracture, the tensile sample exhibited a concave-convex morphology, indicating that the high fraction of FCC phase in the MS24 sample could retard the crack propagation and thereby delay the fracture process.

For further investigation of the fracture behaviour, the microstructures of the side views of the fractured tensile samples of the MS-SS alloys are presented in Fig. 9. For both samples, several cracks and holes across the molten pool tracks can be found. During tensile loading, these cracks and holes accommodated the plastic deformation. For MS12 alloy, only a few elliptical holes can be found on the side surface of the fractured samples. Moreover, the enlarged view in Fig. 9b exhibits a relatively flat fracture surface. For MS24 alloy, it is evident that the cracks and holes were relatively narrower and more prolonged, suggesting a higher resistance to crack propagation during tensile tests. More importantly, the enlarged view in Fig. 9d revealed that a wavy crack propagation path and a large number of dimples were obtained in MS24 alloy. The propagation path extends across a large number of cells, indicating that the high fraction of the FCC phase distributed in the inter-cellular/dendritic regions can retard the crack propagation,

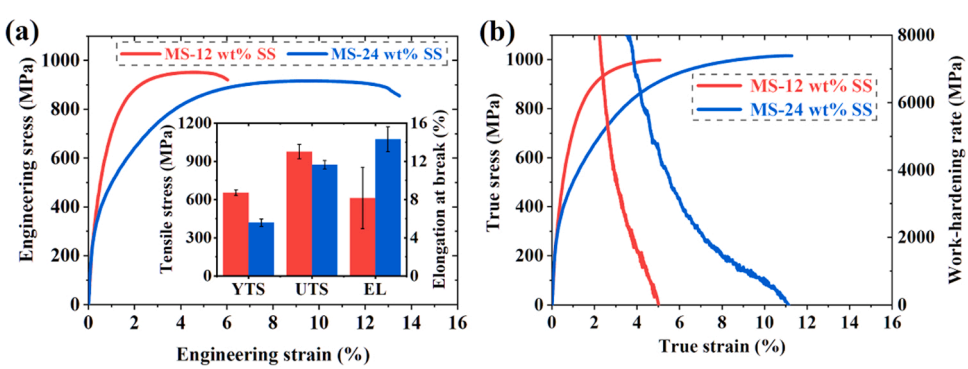

Fig. 7. Tensile properties and deformation behaviour of the MS-SS samples. (a) Engineering stress-strain curves and corresponding tensile data, (b) True stress-strain curves and work-hardening rate curves of the MS-SS samples.

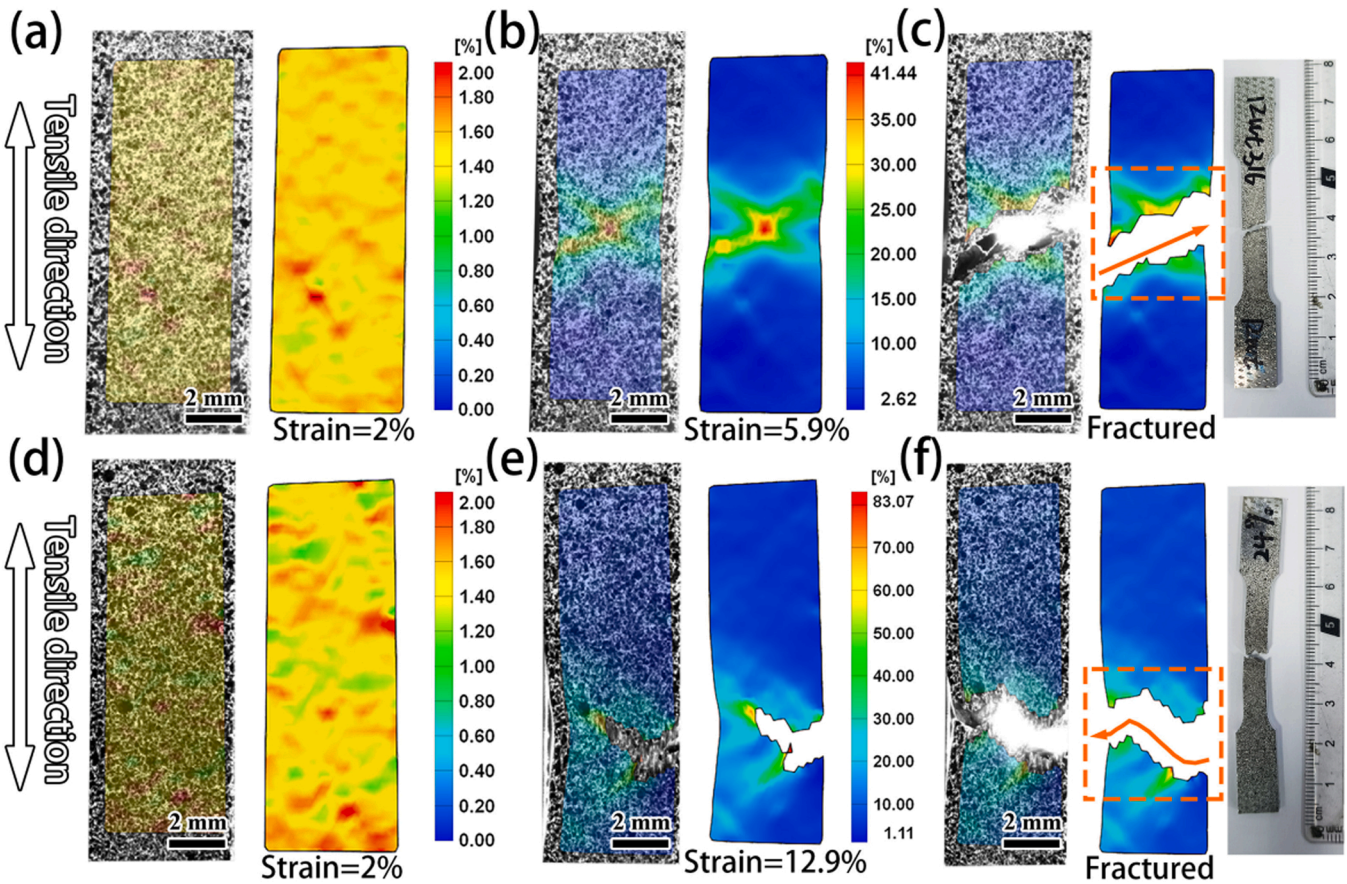

Fig. 8. DIC strain maps and deformation behaviour of (a-c) MS12 and (d-f) MS24 samples during tensile tests.

postponing the fracture process.

4. Discussion

The martensite-austenite DP steels with the heterostructured distribution of the FCC phase were achieved through in-situ alloying MS with SS, and the FCC phase fraction is found to increase proportionally with an increasing amount of SS addition. The formation of BCC/FCC dual-phase microstructure is strongly related to the $\gamma \rightarrow \alpha'$ martensite transformation [24]. According to the empirical formula proposed by Liu et al. [25]:

$$Ms \quad (℃) = 525 - 350(C - 0.005) - 45Mn - 30Cr - 20Ni - 16Mo - 5Si + 6Co \tag{1}$$

The start temperature of martensite transformation (*Ms*) of MS12 and MS24 alloy were estimated to be 97.3 and 56.2 ℃, respectively. The difference in *Ms* of the two types of steels was mainly attributed to the introduction of austenite stabilising elements (e.g., Cr and Mn). Compared with typical martensite steel, the *Ms* of two novel MS-SS steels was relatively low, which promoted the formation of martensite-austenite dual-phase microstructure. Moreover, the columnar γ grains formed in MS24 alloy (Fig. 6a) can also be attributed to its low *Ms* (56.2 ℃). Due to the low *Ms*, the occurrence of martensite transformation is not sufficient to eradicate the columnar grains formed during the solidification of the melt pools [13]. In addition, according to the phase distribution map and corresponding EDS results, the FCC phase formation seems to correlate well with the micro-segregation of Mo. A similar phenomenon has also been reported in an LPBF-processed 18-Ni300 maraging steel, in which the retained austenite usually exists in the Ti/Mo/Ni enriched inter-cellular/dendritic regions [26]. According to Eq. (1), it can be inferred the micro-segregation of Mo in the inter-cellular/dendritic region could decrease the localised *Ms* and retard the martensite transformation, thereby stabilising the FCC phase.

The geometrically necessary dislocations (GND) maps and GND density distributions of two types of steels were presented in Fig. 10a-d. For the two types of steels, the GND density of the FCC phase was almost the same. However, the GND density of the BCC phase in the MS12 alloy (8.05×10^{14} m^{-2}) was obviously higher than that in the MS24 alloy (7.77×10^{14} m^{-2}). The particular phenomenon can be attributed to the following factors. During martensite transformation, numerous dislocations were generated within the martensite phase to accommodate the transformation strain, and the cooling rate at *Ms* is the dominant factor affecting the dislocation density in the martensite phase [27,28]. Due to the *Ms* of MS24 alloy being only 56.2 ℃, it can be inferred the cooling rate at *Ms* of MS24 alloy is relatively lower than that of MS12 alloy due to the thermal accumulation during LDED deposition and slow heat dispersion at low temperature, which lowers the dislocation density. More importantly, the lower *Ms* of MS24 alloy will retard the $\gamma \rightarrow \alpha'$ martensite transformation, thereby leading to the columnar γ grains and higher texture intensity of the BCC phase, as shown in Fig. 6. The martensite grain boundaries maps in Fig. 10e and f indicate that the fraction of low angle grain boundaries (LAGB, 2–15°) of MS12 alloy is higher than that of MS24 alloy, which further demonstrates that the dislocation density of martensite in MS24 alloy is lower [29]. Considering the BCC/FCC phase fraction, the gross GND densities of MS12 and MS-24 alloy were estimated to be 7.87×10^{14} m^{-2} and 7.28×10^{14} m^{-2}, respectively.

In terms of the mechanical performance, the higher concentration of SS (24 wt. %) leads to lower yield tensile strength but brings higher work-hardening capability and ductility to the alloy. Compared with MS12 alloy, the lower yield strength of MS24 alloy can be attributed to their lower dislocation density, larger cellular size and a higher fraction

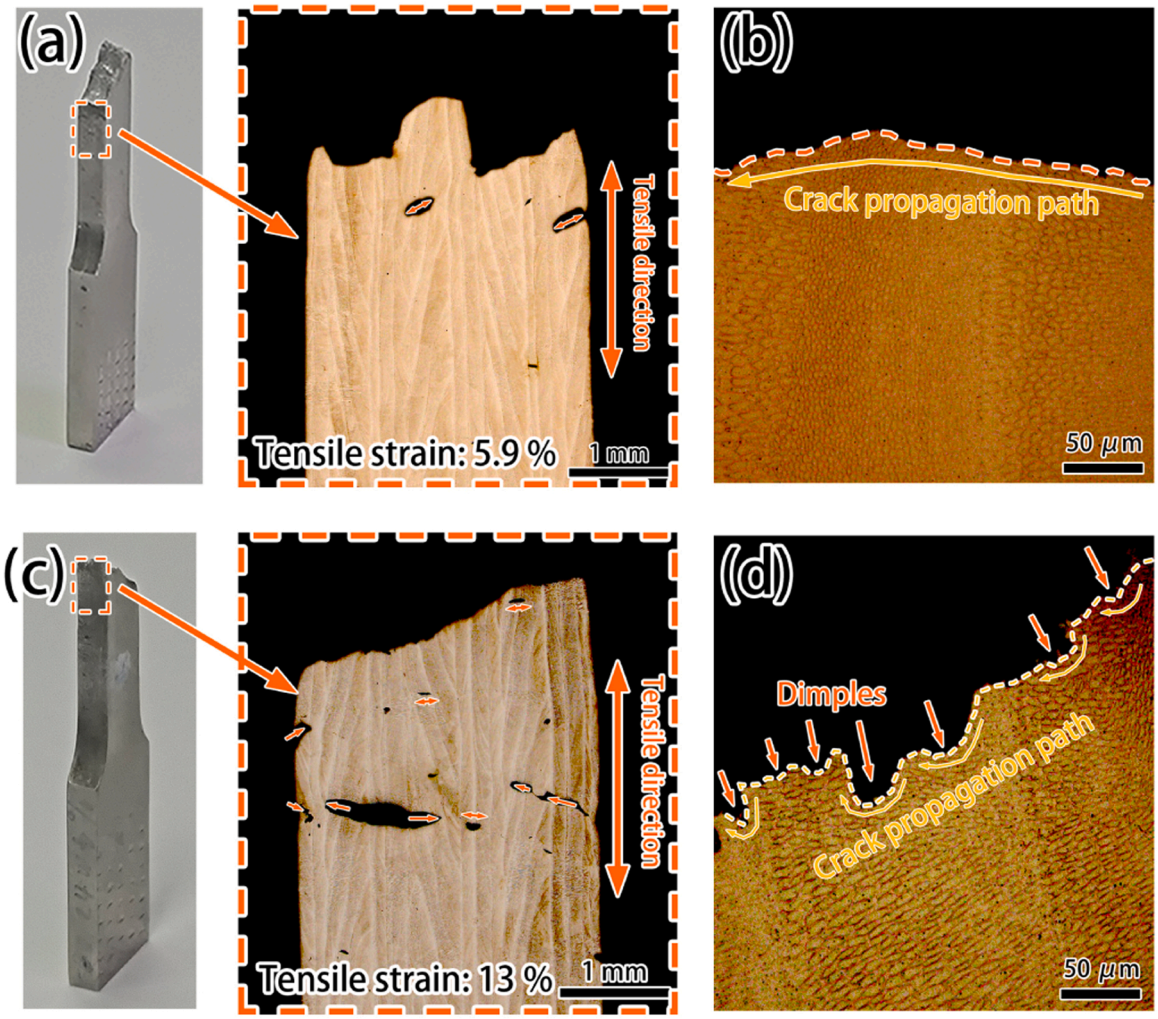

Fig. 9. The side surface of fractured tensile samples of (a-b) MS12 and (c-d) MS24 alloys.

of FCC phase. However, the ultimate tensile strength of the two alloys does not show an enormous difference, which indicates that a higher work-hardening capability was achieved in the MS24 alloy. As discussed above, the higher work-hardening capability of MS24 alloy originated from the following factors. On one hand, the more evident spatial heterostructured microstructure with alternatively FCC-rich and FCC-lean regions of MS24 alloy leads to the strain partitioning phenomenon (Fig. 8d). The initial plastic strain was mainly located in the softer FCC-rich region, which is favourable for the stable work-hardening stage [30]. On the other hand, the higher content of the FCC phase with low dislocation density enables the accommodation of more dislocations during tensile loading (Fig. 10), thereby contributing to the stable work-hardening behaviour.

5. Conclusions

In conclusion, novel MS-*x*SS ($x = 12$, 24 wt. %) DP steels with heterostructured martensite-austenite dual-phases were fabricated by LDED. The microstructures, mechanical properties and deformation behaviour of the novel DP steels were investigated. The main conclusions are:

(1) The FCC phase fraction increases with the increase of SS content. The fractions of the FCC phase were 5.8 % and 16.8 % in the MS12 and MS24 alloys, respectively. Due to the different thermal histories at the layer/melt pool boundaries and inner melt pools during deposition, spatial heterostructured microstructure with alternative FCC-rich and FCC-lean regions were formed.

(2) The *Ms* of MS12 and MS24 alloy were estimated to be 97.3 and 56.2 ℃, respectively. According to the texture analysis and GND density evaluations, the resistance of $\gamma \rightarrow \alpha'$ transformation becomes more prominent with the incorporation of higher content of SS due to the different *Ms*. Moreover, the micro-segregation of Mo in the inter-cellular/dendritic region could decrease the localised *Ms*, retard the martensite transformation, and stabilise the FCC phase.

(3) Compared with MS12 alloy, MS24 alloy showed a much higher elongation (14.3 %) and a superior work-hardening capability. The in-situ DIC observation revealed the strain partitioning within the two alloys during the initial deformation stage.

CRediT authorship contribution statement

J. Su: Methodology, Formal analysis, Writing – original draft. **C. Tan:** Conceptualization, Supervision, Funding acquisition, Writing – review & editing. **F. Ng**: Methodology. **F. Weng**: Writing – review & editing. **L. Chen**: Investigation. **F. Jiang:** Investigation. **J. Teng:** Formal analysis, Supervision. **Y. Chew:** Writing – review & editing, Resources.

Declaration of Competing Interest

The authors declare that they have no known competing financial

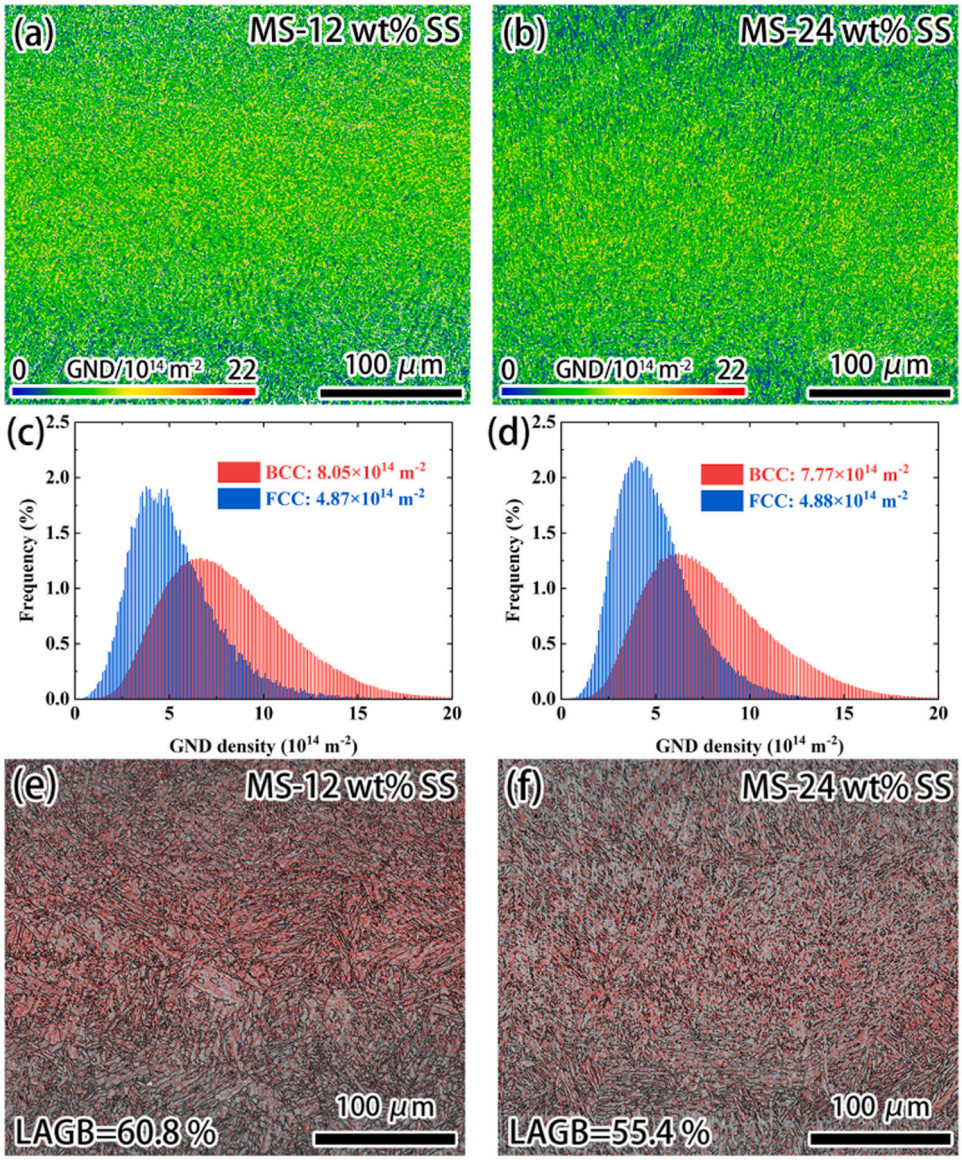

Fig. 10. GND maps and GND density distributions of (a, c) MS12 and (b, d) MS24 alloy, grain boundaries maps of martensite phase of (e) MS12 and (f) MS24 alloy.

interests or personal relationships that could have appeared to influence the work reported in this paper.

Data availability

Data will be made available on request.

Acknowledgements

This research was financially supported by Agency for Science, Technology and Research (A*Star), Singapore, under the Career Development Fund (Grant Nos: C210112051 and C210812047). J. Su acknowledges the sponsorship of the China Scholarship Council, China (No. 202106130051).

References

[1] B. Tomar, S. Shiva, T. Nath, A review on wire arc additive manufacturing: processing parameters, defects, quality improvement and recent advances, Mater. Today Commun. 31 (2022), 103739, https://doi.org/10.1016/j.mtcomm.2022.103739.

[2] C. Tan, Y. Chew, G. Bi, D. Wang, W. Ma, Y. Yang, K. Zhou, Additive manufacturing of steel–copper functionally graded material with ultrahigh bonding strength, J. Mater. Sci. Technol. 72 (2021) 217–222, https://doi.org/10.1016/j.jmst.2020.07.044.

[3] Y. Huang, D. Wu, D. Zhao, F. Niu, G. Ma, Investigation of melt-growth alumina/aluminum titanate composite ceramics prepared by directed energy deposition, Int. J. Extrem. Manuf. 3 (2021), https://doi.org/10.1088/2631-7990/abf71a.

[4] M.H. Mosallanejad, B. Niroumand, A. Aversa, A. Saboori, In-situ alloying in laser-based additive manufacturing processes: a critical review, J. Alloy. Compd. 872 (2021), 159567, https://doi.org/10.1016/j.jallcom.2021.159567.

[5] P. Bajaj, A. Hariharan, A. Kini, P. Kürnsteiner, D. Raabe, E.A. Jägle, Steels in additive manufacturing: a review of their microstructure and properties, Mater. Sci. Eng. A 772 (2020), https://doi.org/10.1016/j.msea.2019.138633.

[6] S.S. Xu, J.P. Li, Y. Cui, Y. Zhang, L.X. Sun, J. Li, J.H. Luan, Z.B. Jiao, X.L. Wang, C. T. Liu, Z.W. Zhang, Mechanical properties and deformation mechanisms of a novel austenite-martensite dual phase steel, Int. J. Plast. 128 (2020), https://doi.org/10.1016/j.ijplas.2020.102677.

[7] B.B. He, H.W. Luo, M.X. Huang, Experimental investigation on a novel medium Mn steel combining transformation-induced plasticity and twinning-induced plasticity effects, Int. J. Plast. 78 (2016) 173–186, https://doi.org/10.1016/j.ijplas.2015.11.004.

[8] B.L. Ennis, E. Jimenez-Melero, E.H. Atzema, M. Krugla, M.A. Azeem, D. Rowley, D. Daisenberger, D.N. Hanlon, P.D. Lee, Metastable austenite driven work-hardening behaviour in a TRIP-assisted dual phase steel, Int. J. Plast. 88 (2017) 126–139, https://doi.org/10.1016/j.ijplas.2016.10.005.

[9] Y. Toji, H. Matsuda, M. Herbig, P.P. Choi, D. Raabe, Atomic-scale analysis of carbon partitioning between martensite and austenite by atom probe tomography

and correlative transmission electron microscopy, Acta Mater. 65 (2014) 215–228, https://doi.org/10.1016/j.actamat.2013.10.064.
[10] D. Zhang, A. Liu, B. Yin, P. Wen, Additive manufacturing of duplex stainless steels - a critical review, J. Manuf. Process. 73 (2022) 496–517, https://doi.org/10.1016/j.jmapro.2021.11.036.
[11] F. Hengsbach, P. Koppa, K. Duschik, M.J. Holzweissig, M. Burns, J. Nellesen, W. Tillmann, T. Tröster, K.-P. Hoyer, M. Schaper, Duplex stainless steel fabricated by selective laser melting - microstructural and mechanical properties, Mater. Des. 133 (2017) 136–142, https://doi.org/10.1016/j.matdes.2017.07.046.
[12] H. Li, S. Thomas, C. Hutchinson, Delivering microstructural complexity to additively manufactured metals through controlled mesoscale chemical heterogeneity, Acta Mater. 226 (2022), https://doi.org/10.1016/j.actamat.2022.117637.
[13] Y. Yin, Q. Tan, M. Bermingham, N. Mo, J. Zhang, M.X. Zhang, Laser additive manufacturing of steels, Int. Mater. Rev. 0 (2021) 1–87, https://doi.org/10.1080/09506608.2021.1983351.
[14] A. Ben-Artzy, A. Reichardt, J.P. Borgonia, R.P. Dillon, B. McEnerney, A.A. Shapiro, P. Hosemann, Compositionally graded SS316 to C300 Maraging steel using additive manufacturing, Mater. Des. 201 (2021), 109500, https://doi.org/10.1016/j.matdes.2021.109500.
[15] D.L. Olson, Prediction of austenitic weld metal microstructure and properties, Weld. J. (Miami Fla). 64 (1985).
[16] C. Tan, Y. Liu, F. Weng, F.L. Ng, J. Su, Z. Xu, X.D. Ngai, Y. Chew, Additive manufacturing of voxelised heterostructured materials with hierarchical phases, Addit. Manuf. 54 (2022), 102775, https://doi.org/10.1016/j.addma.2022.102775.
[17] C. Tan, K. Zhou, M. Kuang, W. Ma, T. Kuang, Microstructural characterisation and properties of selective laser melted maraging steel with different build directions, Sci. Technol. Adv. Mater. 19 (2018) 746–758, https://doi.org/10.1080/14686996.2018.1527645.
[18] G. Yang, F. Deng, S. Zhou, B. Wu, L. Qin, Microstructure and mechanical properties of a novel Cu-reinforced maraging steel for wire arc additive manufacturing, Mater. Sci. Eng. A. 825 (2021), 141894, https://doi.org/10.1016/j.msea.2021.141894.
[19] C. Tan, J. Zou, D. Wang, W. Ma, K. Zhou, Duplex strengthening via SiC addition and in-situ precipitation in additively manufactured composite materials, Compos. Part B Eng. 236 (2022), 109820, https://doi.org/10.1016/j.compositesb.2022.109820.
[20] H. Pirgazi, M. Sanjari, S. Tamimi, B. Shalchi Amirkhiz, L.A.I. Kestens, M. Mohammadi, Texture evolution in selective laser melted maraging stainless steel CX with martensitic transformation, J. Mater. Sci. 56 (2021) 844–853, https://doi.org/10.1007/s10853-020-05290-2.
[21] V.A. Yardley, E.J. Payton, Austenite–martensite/bainite orientation relationship: characterisation parameters and their application, Mater. Sci. Technol. (U. Kingd.). 30 (2014) 1125–1130, https://doi.org/10.1179/1743284714Y.0000000572.
[22] S. Morito, X. Huang, T. Furuhara, T. Maki, N. Hansen, The morphology and crystallography of lath martensite in alloy steels, Acta Mater. 54 (2006) 5323–5331, https://doi.org/10.1016/j.actamat.2006.07.009.
[23] X. Tan, D. Ponge, W. Lu, Y. Xu, X. Yang, X. Rao, D. Wu, D. Raabe, Carbon and strain partitioning in a quenched and partitioned steel containing ferrite, Acta Mater. 165 (2019) 561–576, https://doi.org/10.1016/j.actamat.2018.12.019.
[24] S.A.R. Shamsdini, S. Shakerin, A. Hadadzadeh, B.S. Amirkhiz, M. Mohammadi, A trade-off between powder layer thickness and mechanical properties in additively manufactured maraging steels, Mater. Sci. Eng. A 776 (2020), 139041, https://doi.org/10.1016/j.msea.2020.139041.
[25] C. Liu, Z. Zhao, D.O. Northwood, Y. Liu, A new empirical formula for the calculation of MS temperatures in pure iron and super-low carbon alloy steels, J. Mater. Process. Technol. 113 (2001) 556–562, https://doi.org/10.1016/S0924-0136(01)00625-2.
[26] E.A. Jägle, Z. Sheng, P. Kürnsteiner, S. Ocylok, A. Weisheit, D. Raabe, Comparison of maraging steel micro- and nanostructure produced conventionally and by laser additive manufacturing, Materials (Basel) 10 (2017), https://doi.org/10.3390/ma10010008.
[27] S. Morito, J. Nishikawa, T. Maki, Dislocation density within lath martensite in Fe-C and Fe-Ni alloys, ISIJ Int. 43 (2003) 1475–1477, https://doi.org/10.2355/isijinternational.43.1475.
[28] J. Su, X. Ji, J. Liu, J. Teng, F. Jiang, D. Fu, H. Zhang, Revealing the decomposition mechanisms of dislocations and metastable α' phase and their effects on mechanical properties in a Ti-6Al-4V alloy, J. Mater. Sci. Technol. 107 (2021) 136–148, https://doi.org/10.1016/j.jmst.2021.07.048.
[29] R. Palad, Y. Tian, K. Chadha, S. Rodrigues, C. Aranas, Microstructural features of novel corrosion-resistant maraging steel manufactured by laser powder bed fusion, Mater. Lett. 275 (2020), 128026, https://doi.org/10.1016/j.matlet.2020.128026.
[30] Y. Zhu, K. Ameyama, P.M. Anderson, I.J. Beyerlein, H. Gao, H.S. Kim, E. Lavernia, S. Mathaudhu, H. Mughrabi, R.O. Ritchie, N. Tsuji, X. Zhang, X. Wu, Heterostructured materials: superior properties from hetero-zone interaction, Mater. Res. Lett. 9 (2021) 1–31, https://doi.org/10.1080/21663831.2020.1796836.